Journal of Intelligent and Robotic Systems manuscript No.
(will be inserted by the editor)

A Survey of AM-FM methods for Applications in Medical Imaging

Victor Murray · Eduardo S. Barriga · Marios S. Pattichis · Peter Soliz

Received: date / Accepted: date

Abstract Amplitude-Modulation Frequency-Modulation (AM-FM) decompositions represent images using spatially-varying sinusoidal waves and their spatially-varying amplitudes. The model uses different scales and bandpass filters to characterize the wide range of frequencies that may be present in an image. In the past few years, as the understanding of its theory advanced, AM-FM has been used in a series of medical imaging problems ranging from ultrasound to retinal image analysis, yielding excellent results. This paper summarizes the theory of AM-FM and some of its main medical imaging applications: carotid artery ultrasound, pneumoconiosis, diabetic retinopathy, and age-related macular degeneration.

Keywords Multidimensional AM-FM methods · digital image processing · medical imaging.

1 Introduction

In the field of computer aided detection and diagnostics (CAD), recent advances in image processing techniques have brought a wide array of applications into the field. Many existing CAD methods rely on fixed basis functions based on wavelet decompositions [1] and Gabor filters [2]. Amplitude-Modulation Frequency-Modulation (AM-FM) methods [3–6] represent an emerging technique that shows great promise in this area.

Multi-dimensional AM-FM models and methods provide us with powerful, image and video decompositions that can effectively describe non-stationary content. They represent an extension to standard Fourier analysis, where we allow both the amplitude and the phase functions to vary spatially over the support of the image, following changes in local texture and brightness.

To explain some of the advantages of AM-FM methods, we begin with the basic AM-FM model. In the 2D model, we expand an input image $I(x, y)$ into a sum of AM-FM harmonics using:

$$I(x,y) = \sum_{n=1}^{M} a_n(x,y)\cos\varphi_n(x,y), \tag{1}$$

where $a_n(x, y)$ denote slowly-varying instantaneous amplitude (IA) functions, $\varphi_n(x, y)$ denote the instantaneous phase (IP) components, and $n = 1, 2, \ldots, M$ indexes the different AM-FM harmonics. In (1), we have that the n-th AM-FM harmonic is represented by $a_n(x, y)\cos\varphi_n(x, y)$.

With each phase function, we associate the instantaneous frequency (IF) vector field defined by $\nabla\varphi_n(x, y)$. Here, the AM-FM demodulation problem is defined as one of determining the IA, IP, and IF functions for any given input image. We now have a number of different methods for computing AM-FM decompositions.

AM-FM decompositions provide for physically meaningful texture measurements. Usually, significant texture variations are captured in the frequency components. For single component cases, IF vectors are orthogonal to equi-intensity lines of an image, while the IF magnitude provides a measure of local frequency

V. Murray · M.S. Pattichis
University of New Mexico, Department of Electrical and Computer Engineering, Albuquerque, NM-87131.
Tel.: +1-505-277-2436
Fax: +1-505-277-1439
E-mail: vmurray@ieee.org, pattichis@ece.unm.edu

E.S. Barriga · P. Soliz
VisionQuest Biomedical, Albuquerque, NM-87106.
Tel.: +1-505-508-1994
Fax: +1-505-508-5308
E-mail: sbarriga@visionquest-bio.com, psoliz@visionquest-bio.com

content. In (1), by using AM-FM components from different scales, we can produce IF vectors from different scales, at a pixel-level resolution [4, 5].

Since AM-FM texture features are provided at a pixel-level resolution, AM-FM models can be used to segment texture images that are very difficult to model with the standard brightness-based methods [7]. On the other hand, using just histograms of the IF and IA, we can design effective content-based image retrieval systems using very short image feature vectors [8].

In summary, the advantages of AM-FM methods include [9]: (i) they provide for a large number of physically meaningful texture features, over multiple scales, at a pixel-level resolution, (ii) we can reconstruct the image from the AM-FM decompositions, (iii) based on the target application, we can design for different AM-FM decompositions using different frequency coverage and (iv) we have the recent development of very robust methods for AM-FM demodulation (see some recent examples in [4]).

We can extend AM-FM decompositions for representing videos using [10]:

$$I(x,y,t) = \sum_{n=1}^{M} a_n(x,y,t)\cos\varphi_n(x,y,t), \tag{2}$$

where each AM-FM function has been extended to be a function of both space and time. The original phase-based modeling approach was provided by Fleet and Jepson in [11] and was recently extended by Murray et al. in [10, 11].

The comparison between an AM-FM reconstruction and the original image provides us with a method to better understand what AM-FM is measuring. For continuous-space image decompositions, AM-FM reconstruction examples can be found in [12], while [4, 5] give several recent, robust multi-scale examples for both images and videos. AM-FM Transform examples were shown in [13], while multidimensional orthogonal FM transforms were demonstrated in [14].

An early example of the use of frequency-domain filtering to target a particular application can be found in the fingerprint examples in [15]. More recently, Ramachandran provided a tree-growth application, where inter-ring spacing was used to design filterbanks that cover a specific part of the spectrum, so as to recover tree ring and tree growth structure from very noisy image inputs [16]. For general images, Gabor filterbank approaches were investigated by Havlicek in [3]. Similarly, for general images and videos, Murray introduced dyadic, multiscale decompositions in his dissertation [4].

Alternatively, AM-FM estimates can be obtained using an Energy Separation Algorithm (ESA) as described in [17–19]. Both ESA and Hilbert-based methods share the use of a filterbank prior to AM-FM demodulation. Furthermore, both methods extract estimates from a dominant component. For ESA, the dominant component is selected based on an energy criterion. In QEA, the dominant component is often selected based on IA estimates. In this article, we will only provide details for the Hilbert-based methods focusing on the accurate results presented in [5].

The methods Section 2 describes the theory behind AM-FM and some of the post-processing and classification techniques used. Results are presented for several applications in Section 3. Finally, conclusions and future work are presented on Section 4.

2 Methods

2.1 AM-FM methods

We consider multi-scale AM-FM representations, under least-square approximations, for 2D signals (images) given by

$$I(x,y) \simeq \sum_{n=1}^{M} a_n(x,y)\cos\varphi_n(x,y), \tag{3}$$

where $n = 1, 2, \ldots, M$ denote different scales [4, 5]. In (3), a continuous image $I(x,y)$ is a function of a vector of spatial coordinates (x,y). A collection of M different scales are used to model essential signal modulation structure. The amplitude functions $a_n(\cdot)$ are always assumed to be positive.

AM-FM models non-stationary image content in terms of its amplitude and phase functions [6]. The aim is to let the frequency-modulated (FM) components $\cos\varphi_n(\cdot)$ capture fast-changing spatial variability in the image intensity. For each phase function $\varphi_n(\cdot)$ we define the instantaneous frequency (IF), $\nabla\varphi_n(\cdot)$, in terms of the gradient. We have:

$$\nabla\varphi_n(x,y) = \left(\frac{\partial\varphi_n}{\partial x}(x,y),\ \frac{\partial\varphi_n}{\partial y}(x,y)\right). \tag{4}$$

The instantaneous frequency vector $\nabla\varphi_n(\cdot)$ can vary continuously over the spatial domain of the input signal.

The basic, Hilbert-based AM-FM demodulation system is given in Figs. 1 and 2. First, the real-valued input signal is "analytically" extended by removing all negative frequency components. The effect of this operation is to create a complex-valued signal of the form: $a(x,y)\exp[j\varphi(x,y)]$. We then use a collection of bandpass filters to isolate the individual AM-FM components [3].

The basic assumption here is that different AM-FM components will be picked up by different bandpass filters, at the same image region. In other words, given any local image region, the assumption is that the corresponding AM-FM components will be separated by the use of different filters in the filterbank.

Given the digital input image $I(k_1, k_2)$ (where k_1 and k_2 are the discrete versions of x and y, respectively), we first apply a partial Hilbert transform to form a *2D extension* of the 1D analytic signal: $I_{AS}(k_1, k_2)$. This 2D extension is processed through a collection of bandpass filters (to be described in the subsection 2.2) within the desired scale. Each processing block will produce the instantaneous amplitude, the instantaneous phase, and the instantaneous frequencies in both x and y directions.

For each pixel (pixel-level approach) we select the AM-FM demodulation estimates from the bandpass filter that produces the largest instantaneous amplitude estimate (dominant component analysis, DCA). Hence, the algorithm adaptively selects the estimates from the bandpass filter with the maximum response. This approach does not assume spatial continuity, and allows the model to quickly adapt to singularities in the input signal (both high and low frequency changes).

For any single-scale, the IA and the IP are estimated using [3] $\hat{a}(k_1, k_2) = |\hat{I}_{AS}(k_1, k_2)|$ and $\hat{\varphi}(k_1, k_2) = \arctan\Big(\text{imag}(\hat{I}_{AS}(k_1, k_2))/\,\text{real}(\hat{I}_{AS}(k_1, k_2))\Big)$, respectively, with $\hat{I}_{AS}(k_1, k_2) = I(k_1, k_2) + j\mathcal{H}_{2d}[I(k_1, k_2)]$, where $\mathcal{H}_{2d}$ denotes a two-dimensional partial Hilbert transform operator.

For robust IA and IF estimations, we use a variable spacing, local linear phase (VS-LLP) method as described in [4,5]. Here, for estimating the first component, we generate four estimates using:

$$\hat{\varphi_1}(k_1, k_2) = \frac{1}{n_1} \arccos\left(\frac{\bar{I}_{AS}(k_1 + n_1, k_2) + \bar{I}_{AS}(k_1 - n_1, k_2)}{2\bar{I}_{AS}(k_1, k_2)}\right), \quad (5)$$

where $\bar{I}_{AS}(k_1, k_2) = \hat{I}_{AS}(k_1, k_2)/|\hat{I}_{AS}(k_1, k_2)|$, n_1 represents a variable displacement n_1, from 1 to 4. VS-LLP produces the most accurate of the four estimates by considering the condition number of the arccos$(\cdot)$ function [4, 5]. The approach is similar for the second component direction. It turns out that VS-LLP reduces to the earlier method of Quasi-Eigenfunction Approximation (QEA) for the special case when $n_1 = n_2 = 1$ (see [3] for QEA).

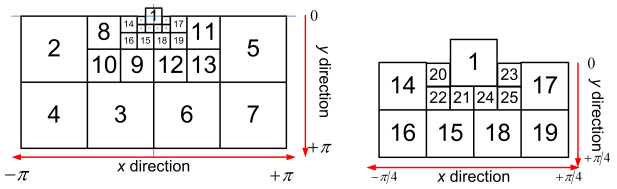

Fig. 2 Four-scale filterbank used. (a) Complete frequency spectrum of the filterbank. (b) Zoom on the low frequency bandpass filters.

2.2 Filterbank Design

For computing the AM-FM estimates, we need to isolate the AM-FM components from (3) using a multiscale filterbank. Here, the basic idea is to isolate different AM-FM components over different frequencies (see [20] for details). Fig. 2 (a) depicts the frequency support for a dyadic filterbank decomposition.

In Fig. 2, the low pass filter (LPF, with label number 1) has frequency support in $[-\pi/16, \pi/16]$ radians for both the x and y directions. The filters in the highest frequencies (filters from 2 to 7 in Fig. 2), have a bandwidth of $\pi/2$ for both x and y directions. The bandwidth is decreased by a factor of 0.5 for each added scale. In Fig. 2 (b), we provide a closeup that shows the low frequency filters.

We define the scales using a collection of bandpass filters as: (i) LPF (lowpass filter), (ii) VL (very low frequencies), (iii) L (low frequencies), (iv) M (medium frequencies) and (v) H (high frequencies) as given in [4]. When the structures are well defined in sizes, the measurements can be related with specific instantaneous wavelengths described in number of pixels [21, 22].

For example, for classifying lung opacities in pneumoconiosis (to be fully described in subsection 3.2), the correspondence between opacity size and instantaneous frequencies using eleven different combinations of scales (CoS) is shown in Table 1. The pneumoconiosis images that were analyzed in the study have a resolution of 300dpi. This resolution means that along 0.5mm we have 6 pixel samples. From the ILO standard [23], the rounded opacities labeled as p, q and r, are in the sizes up to 10mm. With the knowledge of the sizes, we can relate the lengths with the corresponding frequencies. In Table 2 we summarize these relationships. Based on the frequency ranges for each rounded opacity type, we set up the cut-off frequencies of the bandpass filters to fit the opacities in them by each scale. Then, we design our four-scale filter-bank such that each scale will be related with the frequency ranges described in Table 2.

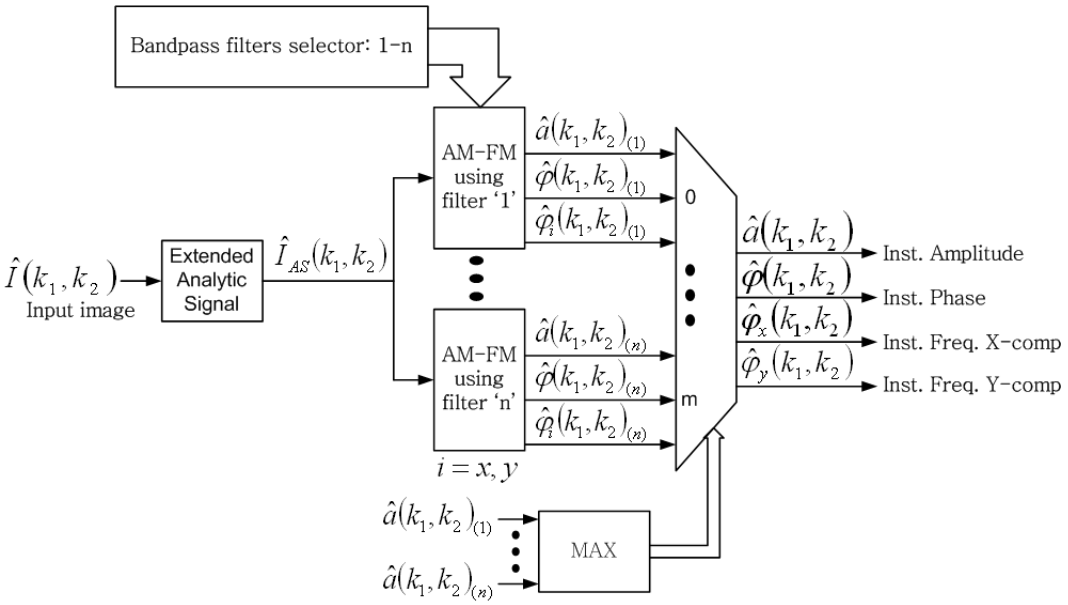

Fig. 1 Block diagram of the 2D multi-scale AM-FM demodulation. Dominant AM-FM components are selected over different image scales. The bandpass filter selector (upper left) is used to define the bandpass filters that correspond to each scale. The dominant AM-FM component is selected using the maximum amplitude at every pixel (see lowest block).

Table 1 Combinations of scales used for computing the dominant AM-FM feature parameters.

CoS*	Scales used	CoS*	Scales used
1	VL, L, M, H	7	LPF, VL
2	LPF	8	VL, L
3	VL	9	L, M
4	L	10	M, H
5	M	11	H
6	LPF, VL, L, M, H		

CoS*: Combination of Scales.

Table 2 Relationship among ILO standard grades for rounded opacities and the size in mm, size in pixels and range in frequency. Relationships are based on a scanning rate of 12 pixels per *mm*. Frequency range refers to the cut-off frequencies that can be used to characterize an opacity [21].

Type of rounded opacities	Range in *mm*	Range in pixels	Range in lowest frequency content
p	Up to 1.5	Up to 18	$[\pi/9, \pi]$
q	1.5 - 3	18 - 36	$[\pi/18, \pi/9]$
r	3 - 10	36 - 120	$[\pi/36, \pi/18]$

2.3 Post-processing Methods

The AM-FM estimates produced with the methods described in the previous subsections can be improved for better classification purposes. In this subsection, we describe first how the AM-FM estimates are encoded as histograms for a region or image. Second, we present the morphology processing applied as part of the post-processing methods.

2.3.1 Histograms processing

For each of the 11 combinations of scales (see Table 1), we create a 96-bin feature vector that contains the AM-FM histograms. Each AM-FM histogram has the information of (32-bin each): (i) the IA, (ii) the IF magnitude and (iii) the IF angle. Thus, each image produces 11 different feature vectors, each one corresponding to one of the 11 different CoS.

Since the AM-FM estimates of neighboring pixels could be affected by noisy estimates, a 9×9 median filter is applied to the output of the IA and IF estimates (see [4, 5, 12]). Median filtering has the effect of smoothing AM-FM estimates.

Due to the ambiguity of the instantaneous frequency vectors (coming from $\cos\varphi(k_1, k_2) = \cos(-\varphi(k_1, k_2))$), we map the IF estimates to two frequency quadrants:

- Instantaneous frequencies $\frac{\partial\varphi_n}{\partial x}(x, y) \geq 0$ and $\frac{\partial\varphi_n}{\partial y}(x, y) \geq 0$ are kept as they are.
- Instantaneous frequencies $\frac{\partial\varphi_n}{\partial x}(x, y) \geq 0$ and $\frac{\partial\varphi_n}{\partial y}(x, y) < 0$ are kept as they are.

– Instantaneous frequencies $\frac{\partial\varphi_n}{\partial x}(x,y) < 0$ and $\frac{\partial\varphi_n}{\partial y}(x,y) < 0$ are mapped to $|\frac{\partial\varphi_n}{\partial x}(x,y)|$ and $|\frac{\partial\varphi_n}{\partial y}(x,y)|$.
– Instantaneous frequencies $\frac{\partial\varphi_n}{\partial x}(x,y) < 0$ and $\frac{\partial\varphi_n}{\partial y}(x,y) \geq 0$ are mapped to $|\frac{\partial\varphi_n}{\partial x}(x,y)|$ and $-|\frac{\partial\varphi_n}{\partial y}(x,y)|$.

Then, the IF histograms are computed.

For the IF angle, given by $\arctan\left(\frac{\partial\varphi_n}{\partial y}(x,y)/\frac{\partial\varphi_n}{\partial x}(x,y)\right)$, we center the histogram around the maximum value using:

$[h] \leftarrow$ histogram (IF angle using l bins) {Where h is a column vector.}
$H \leftarrow [hhh]$. {Triplicate version of h.}
$i \leftarrow$ Location of the maximum value of h.
$h \leftarrow H_{l+i-l/2+1:l+i+l/2}$.

As last step, all the computed histograms (IA, IF magnitude and IF angle) are normalized such that the cumulative sum of each one is equal to 1. Thus, the bins will now correspond to PDF estimates.

2.4 Partial Least Squares Classification

Partial Least Squares (PLS) is a linear regression method that has been used to create a classifier using the AM-FM features extracted from medical images. The regression problem is given by

$$y = X\beta + \varepsilon, \tag{6}$$

where y is a $n\times 1$ vector of the classification variables, X is a $n\times p$ matrix of the extracted AM-FM features, β is a $p\times 1$ vector of regression weights, and ε is a $n\times 1$ vector of residuals. The least squares solution to estimating β is given by the normal equations $\beta = (X^TX)^{-1}(X^Ty)$.

In our case, we have much more features than images ($p < n$), and AM-FM features in X are highly correlated. Thus, X^TX will be singular or nearly singular and a unique solution to the normal equations does not exist. PLS reduces X to a lower dimensional subspace ($k \ll p$). The first step is to factor X as $X = TL$, where T is an orthogonal $n \times k$ matrix of T-scores and L is a $k \times p$ matrix of factor loadings. The T-scores matrix are used to find a threshold for a classifier [24].

2.5 Morphological segmentation

AM-FM features can also be used for image segmentation. A simple Bayesian classification scheme based on the IA and IF magnitude was demonstrated in [7].

The segmented AM-FM regions can be very noisy. Segmentation region denoising is achieved via the use of an alternating sequential filter (ASF) [25]. We assume that the noise in the segmented image is due to small structural components that do not belong to the abnormal regions. Under this assumption, it can be shown that the optimal morphological filter will be an ASF defined by:

$$M = (((((((I_S \circ B) \bullet B) \circ 2B) \bullet 2B)\ldots) \circ nB) \bullet nB), \tag{7}$$

where: I_S is the binary segmented image, B is the structural element; nB the result of n dilations of B by itself; $\circ$ the standard open operation and $\bullet$ the standard close operation.

The value of n needs to be chosen so that the smaller, noisy structures are removed, while the larger structures are preserved. Once the order of the morphological filter is calculated, the segmented image is denoised using (7).

3 Applications

We provide a selected list of AM-FM biomedical imaging applications in Table 3. We have a number of medical applications based on energy operators. In one of the earlier applications in electron microcopy, a simple Bayesian method using the IA and the IF was used, in conjunction with morphological filtering to provide segmentations of different abnormalities over 26 images [7]. Elshinawy et al. [26] demonstrated the reconstruction of breast cancer images using AM-FM components.

Boudraa et al. [27] introduced a new cross-energy operator and used the operator to demonstrate the functional segmentation of dynamic nuclear images. Maragos et al. provide an important application in [28], where AM-FM models are used for improving Doppler ultrasound resolution. Vector-valued based AM-FM demodulation is given in [29].

Hilbet-based AM-FM methods were used recently applied to medical imaging problems such as chest radiographs [21, 22], ultrasound images of carotid artery [30–32], retinal images [8,33,34], and electron microscopy [7].

AM-FM methods are being applied to different medical applications for not only 2D signals images but also for 1D signals. Only in the last two years, there have been 1D signal applications based on AM-FM methods [35–38], for the classification of surface electromyographic signals [30], brain rhythms in electroencephalograms [39]. We will not summarize 1D applications. We do note that the general AM-FM methodology is also closely related to traditional time-frequency analysis.

For 2D medical applications, related work includes the work by Pattichis [9] where he describes AM-FM methods and models for biomedical image computing, image retrieval in ophthalmology [40], tracking [41–43] and analysis [44, 45].

3.1 Retinal Image Analysis

Diabetic retinopathy (DR) and age-related macular degeneration (AMD) are two retinal diseases that present particular characteristics (lesions) on retinal photographs which can be used in early detection and/or classification of the disease. DR and AMD affect individuals in their most productive years of life. Early detection that leads to prevention of vision loss, alone, will lead to significant decrease in risk of early vision loss.

According to the National Eye Institute, diabetic retinopathy (DR) is one of the leading causes of blindness among working-age Americans, while macular degeneration is a leading cause of blindness among older Americans [57]. It has been shown that regular comprehensive eye exams and timely treatment can lead to improved outcomes and reduced loss of vision. However, to screen the tens of millions at risk for DR would tax the health-care system beyond capacity. Results of an automatic DR screening system based on AM-FM exhibit strong promise in addressing this problem.

Age-related macular degeneration (AMD) is the most common cause of visual loss in the United States and is a growing public health problem. One third of Americans will develop AMD in their lifetimes. To detect AMD, retinal images are graded using the Age-related Eye Disease Study (AREDS) protocol for human grading. AM-FM has been used to develop an automated system for characterizing pathological features on these images.

3.1.1 Diabetic Retinopathy

AM-FM has been used to characterize retinal images with DR, and to screen out patients with different levels of the disease. Fig. 3 shows an image of a retina with DR and one of its IA image.

The types of lesions that need to be detected by the system are shown in Fig. 4. Agurto et al. [33, 58] presented the extraction of Amplitude-Modulation Frequency-Modulation (AM-FM) features for classification of DR images using 376 images from the MESSIDOR database [59].

These 376 images were processed with AM-FM and were divided in two groups for training and testing purposes. Table 4 shows the number of images per risk in each group. The most severe level of DR is grade 3, in which 15 or more microaneurysms or 5 or more hemorrhages are present. For grade 2, the number of microaneurysms in the retina is between 5 and 15 and for grade 1 the retinal images contain between 1 and 5 microaneurysms. The grade 0 corresponds to diabetic patients with no apparent DR in the image. It is important to mention that the images not only contain red lesions such as microaneurysms and hemorrhages, but also contain bright lesions such as exudates and cotton-wool spots.

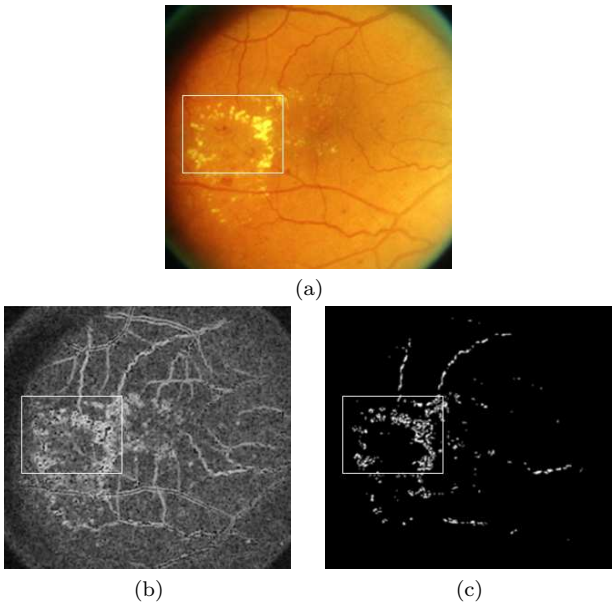

Fig. 3 Example of a retinal image with DR. Note the exudates shown with a white square. (a) Original Retinal Image. (b) Instantaneous Amplitude using CoS 4. (c) Thresholded Image of (b) showing large IA values. A valid range for the pixels between [15% - 30%] of the maximum value was used for determining the thresholded image.

After all the images were processed with AM-FM, they were divided in regions of 100x100 pixels avoiding the optic disc. We calculate as feature vectors the moments in each region: mean, standard deviation, skewness, and kurtosis. Finally, the information per image is the input for the PLS algorithm were the algorithm is trained to classify normal images vs abnormal images.

The results obtained with this approach show an area under the ROC curve of 0.84 with best sensitivity/specificity of 92%/54%. Table III shows the number of images correctly classified per risk level. On this table we can see a large percentage of the high-risk patients are being classified correctly.

3.1.2 Age-Related Macular Degeneration

Barriga et al. [34] have developed a system based on AM-FM to generate multi-scale features for classify-

Table 3 Select list of AM-FM applications in Biomedical Imaging.

Author	Filterbank	AM-FM Demodulation Method	Medical Application
Pattichis et al. 2000 [7]	Gabor filterbank	Quasi-Eigenfunction Approximation (QEA)	Electron microscopy image segmentation
Maragos et al. 2002 [28]	1-D Gabor filterbank	Energy Separation Algorithm (ESA)	Doppler ultrasound spectroscopy resolution
Elshinawy et al. 2004 [26]	Gabor filterbank	QEA and continuous-space demodulation	Demonstrated AM-FM reconstructions of breast cancer images
Boudraa et al. 2006 [27]		Cross Ψ_B energy operator	Nuclear cardiac sequences for one normal and four abnormal cases
Alexandratou et al. 2006 [29]	Gabor filterbank	Vector-valued ESA for color images	Ploidy image analysis (cancer).
Murray et al. 2007 [46]	Dyadic 3D filterbank (optimal design)	QEA + new AM and FM motion estimation	Motion Estimation for Atherosclerotic Plaque videos compared against other Phased-based method
Murray et al. 2008 [8], Agurto et al. 2008 [33] and Barriga et al. [34]	Dyadic 2D filterbank	New variable spacing, local linear phase (VS-LLP) method	Retinal image analysis.
Pitris et al. 2009 [47–49]	Gabor	QEA	Optical coherence tomography.
Rodriguez et al. 2002-2006 [50–52]	Dyadic 2D filterbank	QEA implementation using SIMD	Cardiac applications including Wireless Transmission.
Gill et al. 2005 [53]		1-D monocomponent AM-FM	Detection and identification of heart sounds.
Ramachandran et al. 2001 [54, 55], Pattichis et al. 2002 [56] and Murray et al. 2009 [21, 22]	Polynomial 2D filterbank [54–56] and Dyadic 2D filterbank (optimal design) [21, 22]	Hilbert-based AM-FM	Analysis of pneumoconiosis X-Ray images.
Nguyen et al. 2008	1-D filters and Kalman filters	1-D Hilbert based AM-FM	Analysis of Electroencephalography.
Christodoulou et al. 2009 [30, 31] and Loizou et al. 2009 [32]	Dyadic 2D filterbank	New VS-LLP method	Segmentation and classification in the carotid artery.

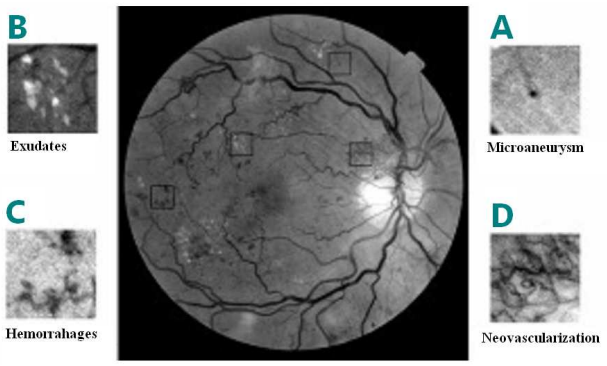

Fig. 4 Lesions typical of a DR retinal image. A) Microaneurysm B) Exudates C) Hemorrahages D) Neovascularization.

Table 4 Images correctly classified per risk. Risk 0 has no DR while Risk 3 images present the most amount of lesions.

Risk	Number	Percentage (%)
3	68	97
2	32	82
1	8	89
0	38	54

ing pathological structures, such as drusen, on a retinal image. Drusen are subretinal deposits characteristic of AMD. Fig. 5 shows an AMD patient with soft and hard drusen present (white spots on the fundus). The standard high-resolution AREDS images were downloaded from the Wisconsin Fundus Photo Reading Center's website [60]. A certified ophthalmic technician (reader) selected the retinal features. For these studies, only areas that contain retinal background, vessels, soft drusen, and hard drusen were used. After the reader selected

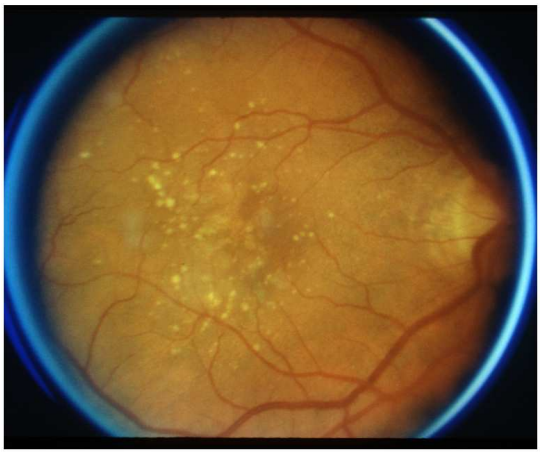

Fig. 5 Retinal image from AMD patient from the AREDS standard database.

Table 5 Mahalanobis distance between retinal features: Retinal Background (RB), Hard Drusen (DRH), Soft Drusen (DRS), and Vessels.

	RB	**DRH**	**DRS**	**Vessels**
RB	-	3.37	5.56	5.34
DRH	-	-	2.82	4.42
DRS	-	-	-	4.50
Vessels	-	-	-	-

the features, regions of interest (ROI) of 40x40 pixels were extracted from the image.

After calculating the AM-FM histograms, principal components analysis (PCA) was applied to the matrix containing histograms of the 120 ROIs (30 for each retinal structure) for three different AM-FM features: IA, IF magnitude (|IF|), and IF angle. Finally, the Mahalanobis distances between the different retinal structures based on PCA decomposition were calculated. These distances are shown in Table 5.

The numbers in Table 5 represent the standard deviations separating the histograms of the retinal structures. The entries under DRH (hard drusen) and DRS (soft drusen) show that they are significantly differentiated from other structures in the retina. A distance of 3 standard deviations represents a classification accuracy of $> 90\%$. The most interesting entry is the Mahalanobis distance between the two drusen types (2.8 standard deviations). Though still considered a high classification rate (85%), this demonstrates the challenge not only to the algorithm, but for the grader in unequivocally assigning drusen to one class or another.

3.2 Pneumoconiosis in chest radiographs

The chest radiograph is an essential tool used in the screening, surveillance, and diagnosis of dust-related respiratory illness resulting from silica and coal dust, asbestos, and a variety of other dusts that can lead to disease. The standardized method used by the International Labor Organization (ILO, [23]) for interpreting the chest radiograph for inorganic dust-induced diseases or pneumoconioses has been widely utilized for the past five decades.

Two limitations of the current ILO system are the intra- and inter-interpreter variability and the time consuming process of interpreting large numbers of radiographs taken for screening and surveillance programs. Murray et al. [21,22] have developed a technique based on AM-FM that detects the level of pneumoconioses based on the nodule formation on the lungs.

Currently, the US remains 6th in the world for pneumoconiosis and interstitial lung disease (ILD) or pulmonary interstitial fibrosis as large numbers of workers continue to be exposed to dust in their work environment. Coal workers' pneumoconiosis (CWP) is identified by a specific pattern of X-Ray abnormalities and a history of exposure to coal dust. The chest radiograph is the single most useful tool for clinically evaluating both occupationally related and non-occupational chronic lung diseases. The chest radiograph is an essential tool used in the screening, surveillance, and diagnosis of dust-related respiratory illness resulting from silica and coal dust, asbestos, and a variety of other dusts that can lead to disease.

We presented in [21,22] an AM-FM method for grading chest radiographs according to the ILO standards. Related work can be found in [55, 56, 61–65]. First, a logarithmic transformation to the images is applied to improve the contrast of the X-Rays [54]. Then, the AM-FM estimates of each X-Ray image is encoded using their histograms as described in the subsection 2.3.1 using the tuned bandpass filters and scales showed in Tables 1 and 2. The final classification was computed using the linear regression method PLS (described in subsection 2.4).

The results obtained by the system were excellent (area under the ROC curve, AUC = 1.0). However, the significance of the results should be debated based on the small database used. The authors plan as future work the testing of the system using a much bigger database. The authors produced classification results that were significantly better than those presented in [55, 56, 64].

3.3 Carotid Artery Ultrasound images

Cardiovascular disease (CVD) is the third leading cause of death and adult disability in the industrial world after heart attack and cancer. Of all the deaths caused by CVD among adults aged 20 and older, an estimated 6 millions are attributed to coronary heart disease and to stroke, with atherosclerosis as the underlying cause [30–32].

A method based on image analysis of ultrasound images of carotid plaques that can differentiate between the stable plaques that tend to remain asymptomatic and the unstable ones that eventually produce symptoms has the potential to refine the basis for surgery and spare some patients from an unnecessary costly operation which itself carries a risk of stroke.

AM-FM methods are being applied for characterizing and analyzing plaques in ultrasound images. Christodoulou et al. present in [31] their investigations for the AM-FM characterization of carotid plaques in ultrasound images. In [32], Loizou et al. present how to use AM-FM features for describing atherosclerotic plaque features. In what follows, we described the basics of their approaches.

The extraction of features characterizing efficiently the structure of ultrasound carotid plaques is important for the identification of individuals with asymptomatic carotid stenosis at risk of stroke. Christodoloulou et al. present how to characterize the carotid plaques using AM-FM features in [31]. They use as basic descriptors the information about the AM-FM estimates similar as in the subsection 2.3.1: the IA, IF magnitude and IF angle histograms. In addition to the AM-FM features, the authors compute Spatial Gray Level Dependence Matrices (SGLDM) computing the following texture measures: (i) angular second moment, (ii) contrast, (iii) correlation, (iv) sum of squares: variance, (v) inverse difference moment, (vi) sum average, (vii) sum variance, (viii) sum entropy, (ix) entropy, (x) difference variance, (xi) difference entropy and (xii) information measures of correlation. Also, the Gray Level Difference Statistics (GLDS) are computed: (i) contrast, (ii) angular second moment, (iii) entropy and (iv) mean. The final step applied by the authors corresponds to the statistical k-nearest neighbor (KNN) classifier implemented for different values of k ($k = 1, 3, 5, 7, 9, 11, 13$). The authors applied their method to a database of 274 carotid plaque ultrasound images divided as 137 symptomatic and 137 asymptomatic.
Using the AM-FM estimates, the authors got a classification success up to 71.5% when the three AM-FM estimates and $k = 5$ were used. This result was better than using the textures features SGLDM and GLDS when they got 68.2% of succeed.

Loizou et al. present in [32] an AM-FM analysis as an application for investigating the intima media complex (IMC), media layer (ML) and intima layer (IL) of the common carotid artery (CCA). This study represents the first study for the IMC, IL and ML. Clinically, the intima-media thickness (IMT) is used as a validated measure for the assessment of atherosclerosis, that causes enlargement of the arteries and thickening of the artery walls. The authors use the same AM-FM histograms as in subsection 2.3.1 but computed using only horizontal-oriented bandpass filters. Thus, the authors use similar scales like those described in Table 1 but using only the filters numbered as (see Fig. 2a): 1 (LPF), 2, 5 (in the H scale), 8, 11 (in the M scale) and 14 and 17 (in the L scale). The reason for the selection of these horizontal-oriented filters is related with the horizontally elongated nature of the atherosclerotic structures. As the last step for the statistical analysis, the authors use the Mann-Whitney rank sum test in order to identify is there are significant differences (SD) or not (NS) between the extracted AM-FM features. The authors use $p < 0.05$ for significant differences and comparison between different age groups.
Their study, performed on 100 ultrasound images, reveals that the IA of the media layer decreases with age. The authors state that the decreasing of the IA is maybe related to the reduction in calcified, stable plaque components and an increase in stroke risk with age. In terms of the IF, the median of this AM-FM estimate of the media layer increases suggesting fragmentation of solid, large plaque components that also increases the risk of stroke.

4 Conclusions and Future Work

This paper has shown the advances in the application of AM-FM to medical imaging. Its ability to represent different frequencies is highly valuable when analyzing structures with spatial and spectral variability. In retinal images, structures such as drusen and microaneurysms have a well-defined shape that gets captured by the higher-frequency scale AM-FM filters, while vessels and hemorrhages are better represented in the lower frequencies. In chest radiographs, nodules can also be well represented using the AM-FM features. The combination of feature extraction and classification using PLS has produced robust systems for the analysis of chest radiographs, where an automatic grading system for pneumoconiosis has been demonstrated on a limited-size database. For diabetic retinopathy, a screening system has been developed and it is currently being tested

on an extensive database for FDA approval.
Future work on AM-FM will be concentrated on developing new scales (compared with the four-scale filterbank showed in Fig. 2) for representation of lower frequencies. Also, a filter design that includes a constraint of the number of coefficients (length in space) will be applied. This approach will have the advantage of not including extra information of lesion shapes when the filters are applied.

References

1. M. Unser, A. Aldroubi, and A. Laine, "Guest editorial: Wavelets in medical imaging," *IEEE Trans. Med. Imag.*, vol. 22, no. 3, pp. 285–288, March 2003.
2. A. Osareh and B. Shadgar, "Retinal vessel extraction using gabor filters and support vector machines," *Communications in Computer and Information Science*, vol. 6, pp. 356–363, November 2009. [Online]. Available: http://www.springerlink.com/content/m38744668m814665
3. J. P. Havlicek, "AM-FM image models," Ph.D. dissertation, The University of Texas at Austin, 1996.
4. Victor Manuel Murray Herrera, "AM-FM methods for image and video processing," Ph.D. dissertation, University of New Mexico, 2008.
5. V. Murray, P. Rodriguez, and M. S. Pattichis, "Multi-scale AM-FM demodulation and reconstruction methods with improved accuracy," *accepted, IEEE Transactions on Image Processing*, 2009.
6. M. S. Pattichis and A. C. Bovik, "Analyzing image structure by multidimensional frequency modulation," *IEEE Transactions on Pattern Analysis and Machine Intelligence*, vol. 29, no. 5, pp. 753–766, 2007.
7. M. Pattichis, C. Pattichis, M. Avraam, A. Bovik, and K. Kyriacou, "AM-FM texture segmentation in electron microscopic muscle imaging," *IEEE Trans. Med. Imag.*, vol. 19, no. 12, pp. 1253–1257, Dec. 2000.
8. V. Murray, M. Pattichis, and P. Soliz, "New AM-FM analysis methods for retinal image characterization," in *Asilomar Conference on Signals, Systems and Computers*, 2008.
9. M. Pattichis, "Multidimensional AM-FM models and methods for biomedical image computing," in *the 34th IEEE Annual International Conference of the Engineering in Medicine and Biology Society*, September 2009.
10. V. Murray and M. S. Pattichis, "AM-FM demodulation methods for reconstruction, analysis and motion estimation in video signals," in *IEEE Southwest Symposium on Image Analysis and Interpretation*, vol. 0. Los Alamitos, CA, USA: IEEE Computer Society, 2008, pp. 17–20.
11. D. J. Fleet and A. D. Jepson, "Computation of component image velocity from local phase information," *Int. J. Comput. Vision*, vol. 5, no. 1, pp. 77–104, 1990.
12. J. Havlicek, P. Tay, and A. Bovik, *Handbook of Image and Video Processing*. Elsevier Academic Press, 2005, ch. AM-FM Image Models: Fundamental Techniques and Emerging Trends, pp. 377–395.
13. M. Pattichis and A. Bovik, "AM-FM expansions for images," in *Proc. European Signal Processing Conference*, September 1996.
14. M. Pattichis, A. Bovik, J. Havlicek, and N. Sidiropoulos, "Multidimensional orthogonal fm transforms," *IEEE Transactions on Image Processing*, vol. 10, no. 3, pp. 448–464, Mar 2001.
15. M. Pattichis, G. Panayi, A. Bovik, and H. Shun-Pin, "Fingerprint Classification using an AM-FM model," *IEEE Transactions on Image Processing*, vol. 10, no. 6, pp. 951–954, June 2001.
16. J. Ramachandran, "Image analysis of wood core using instantaneous wavelength and frequency modulation," Ph.D. dissertation, University of New Mexico, 2008.
17. P. Maragos, J. F. Kaiser, and T. F. Quatieri, "On amplitude and frequency demodulation using energy operators," *IEEE Transactions on Signal Processing*, vol. 41, no. 4, pp. 1532–1550, April 1993.
18. ——, "Energy separation in signal modulations with applications to speech analysis," *IEEE Transactions on Signal Processing*, vol. 41, no. 10, pp. 3024–3051, October 1993.
19. P. Maragos and A. C. Bovik, "Image demodulation using multidimensional energy separation," *J. Opt. Soc. Am. A*, vol. 12, no. 9, pp. 1867–1876, 1995. [Online]. Available: http://josaa.osa.org/abstract.cfm?URI=josaa-12-9-1867
20. V. Murray, P. Rodriguez V., and M. S. Pattichis, "Robust multiscale AM-FM demodulation of digital images," in *IEEE International Conference on Image Processing*, vol. 1, October 2007, pp. 465–468.
21. V. Murray, M. S. Pattichis, H. Davis, E. S. Barriga, and P. Soliz, "Multiscale AM-FM analysis of pneumoconiosis x-ray images," in *IEEE International Conference on Image Processing*, November 2009.
22. V. Murray, M. S. Pattichis, and P. Soliz, "Retrieval of X-Ray images with different grades of opacities using multiscale am-fm methods," in *Asilomar Conference on Signals, Systems and Computers*, 2009.
23. International Labour Office, *Guidelines for the use of ILO International Classification of Radiographs of Pneumoconioses*, Geneva, Switzerland, 1980.
24. M. Barker and W. Rayens, "Partial least squares for discrimination," *Journal of Chemometrics*, vol. 17, no. 3, pp. 166–173, 2003.
25. D. Schonfeld and J. Goutsias, "Optimal morphological pattern restoration from noisy binary images," *IEEE Trans. Pattern Anal. Mach. Intell.*, vol. 13, no. 1, pp. 14–29, Jan. 1991.
26. M. Y. Elshinawy, J. Zeng, S.-C. B. Lo, and M. F. Chouikha, "Breast cancer detection in mammogram with am-fm modeling and gabor filtering," in *Proc. 7th International Conference on Signal Processing*, vol. 3, Aug. 31–Sep. 4, 2004, pp. 2564–2567.
27. A.-O. Boudraa, J.-C. Cexus, and H. Zaidi, "Functional segmentation of dynamic nuclear images by cross-ψ_b-energy operator," *Computer Methods and Programs in Biomedicine*, vol. 84, no. 2-3, pp. 146 – 152, 2006, medical Image Segmentation Special Issue. [Online]. Available: http://www.sciencedirect.com/science/article/B6T5J-4M3J0J4-2/2/8de02692916912569 43ff4a2409b5588
28. P. Maragos, T. Loupas, and V. Pitsikalis, "Improving doppler ultrasound spectroscopy with multiband instantaneous energy separation," in *Proc. 14th International Conference on Digital Signal Processing*, vol. 2, Jul. 1–3, 2002, pp. 611–614.
29. E. Alexandratou, A. Sofou, H. Papasaika, P. Maragos, D. Yova, and N. Kavantzas, "Computer vision algorithms in DNA ploidy image analysis," in *Proc. of the SPIE Imaging, Manipulation, and Analysis of Biomolecules, Celss, and Tissues*, ser. IV, D. L. Farkas, D. V. Nicolau, and R. C. Leif, Eds., vol. 6088, no. 1. SPIE, 2006, pp. 180–190. [Online]. Available: http://link.aip.org/link/?PSI/6088/60880O/1
30. C. Christodoulou, P. Kaplanis, V. Murray, M. Pattichis, and C. Pattichis, "Classification of surface electromyographic signals using AM-FM features," in *19th International Conference on Artificial Neural Networks*, Limassol, Cyprus, 2009.

31. C. I. Christodoulou, C. Pattichis, V. Murray, M. Pattichis, and A. Nicolaides, "AM-FM representations for the characterization of carotid plaque ultrasound images," in *4th European Conference of the International Federation for Medical and Biological Engineering*, vol. 22, 2009, pp. 546–549. [Online]. Available: http://www.springerlink.com/content/m75t710245211858
32. C. P. Loizou, V. Murray, M. S. Pattichis, C. S. Christodoulou, M. Pantziaris, A. Nicolaides, and C. S. Pattichis, "AM-FM texture image analysis of the intima and media layers of the carotid artery," in *19th International Conference on Artificial Neural Networks*, Limassol, Cyprus, September 2009.
33. C. Agurto, S. Murillo, V. Murray, M. Pattichis, S. Russell, M. Abramoff, and P. Soliz, "Detection and phenotyping of retinal disease using AM-FM processing for feature extraction," in *Asilomar Conference on Signals, Systems and Computers*, 26–29 Oct. 2008, pp. 659–663.
34. E. Barriga, V. Murray, C. Agurto, M. Pattichis, S. Russell, M. Abramoff, H. Davis, and P. Soliz, "Multi-scale AM-FM for lesion phenotyping on age-related macular degeneration," in *IEEE International Symposium on Computer-Based Medical Systems*, Albuquerque, New Mexico, August 2009.
35. T. Ezzat, J. Bouvrie, and T. Poggio, "AM-FM demodulation of spectrograms using localized 2d max-gabor analysis," in *Proc. IEEE International Conference on Acoustics, Speech and Signal Processing ICASSP 2007*, vol. 4, 2007, pp. IV–1061–IV–1064.
36. F. Gianfelici, C. Turchetti, and P. Crippa, "Multicomponent AM-FM demodulation: The state of the art after the development of the iterated hilbert transform," in *IEEE International Conference on Signal Processing and Communications ICSPC 2007*, 2007, pp. 1471–1474.
37. N. Wang, E. Ambikairajah, B. Celler, and N. Lovell, "Feature extraction using an AM-FM model for gait pattern classification," in *Proc. IEEE Biomedical Circuits and Systems Conference BioCAS 2008*, 2008, pp. 25–28.
38. H. Li, L. Fu, and Z. Li, "Fault detection and diagnosis of gear wear based on teager-huang transform," in *Proc. International Joint Conference on Artificial Intelligence JCAI '09*, 2009, pp. 663–666.
39. D. P. Nguyen, R. Barbieri, M. A. Wilson, and E. N. Brown, "Instantaneous frequency and amplitude modulation of EEG in the hippocampus reveals state dependent temporal structure," in *Proc. 30th Annual International Conference of the IEEE Engineering in Medicine and Biology Society EMBS 2008*, 2008, pp. 1711–1715.
40. S. Acton, P. Soliz, S. Russell, and M. Pattichis, "Content based image retrieval: The foundation for future case-based and evidence-based ophthalmology," in *Proc. IEEE International Conference on Multimedia and Expo*, 2008, pp. 541–544.
41. R. Prakash and R. Aravind, "Modulation-domain particle filter for template tracking," in *Proc. 19th International Conference on Pattern Recognition ICPR 2008*, 2008, pp. 1–4.
42. R. Senthil Prakash and R. Aravind, "Invariance properties of AM-FM image features with application to template tracking," in *Proc. Sixth Indian Conference on Computer Vision, Graphics & Image Processing ICVGIP '08*, 2008, pp. 614–620.
43. N. Mould, C. Nguyen, and J. Havlicek, "Infrared target tracking with AM-FM consistency checks," in *Proc. IEEE Southwest Symposium on Image Analysis and Interpretation SSIAI 2008*, 2008, pp. 5–8.
44. I. Kokkinos, G. Evangelopoulos, and P. Maragos, "Texture analysis and segmentation using modulation features, generative models, and weighted curve evolution," *IEEE Trans. Pattern Anal. Mach. Intell.*, vol. 31, no. 1, pp. 142–157, 2009.
45. P. Tay, "AM-FM image analysis using the hilbert huang transform," in *Proc. IEEE Southwest Symposium on Image Analysis and Interpretation SSIAI 2008*, 2008, pp. 13–16.
46. V. Murray, S. E. Murillo, M. S. Pattichis, C. P. Loizou, C. S. Pattichis, E. Kyriacou, and A. Nicolaides, "An AM-FM model for motion estimation in atherosclerotic plaque videos," in *41st Asilomar Conference on Signals, Systems and Computers*, Nov. 4–7, 2007, pp. 746–750.
47. C. Pitris, A. Kartakoullis, and E. Bousi, "AM-FM techniques in the analysis of optical coherence tomography signals," *Journal of Biophotonics*, vol. 2, no. 6-7, pp. 364–369, 2009.
48. A. Kartakoulis, E. Bousi, and C. Pitris, "AM-FM analysis of optical coherence tomography signals," in *Optical Coherence Tomography and Coherence Domain Optical Methods in Biomedicine XIII*, J. G. Fujimoto, J. A. Izatt, and V. V. Tuchin, Eds., vol. 7168, no. 1. SPIE, 2009, p. 71681M. [Online]. Available: http://link.aip.org/link/?PSI/7168/71681M/1
49. A. Kartakoullis, E. Bousi, and C. Pitris, "AM-FM techniques in optical coherence tomography," in *Optical Coherence Tomography and Coherence Techniques IV*, P. E. Andersen and B. E. Bouma, Eds., vol. 7372, no. 1. SPIE, 2009, p. 73720U. [Online]. Available: http://link.aip.org/link/?PSI/7372/73720U/1
50. P. Rodriguez V. and M. S. Pattichis, "Nested random phase sequence sets: a link between AM-FM demodulation and increasing operators with application to cardiac image analysis," in *Proc. 6th IEEE Southwest Symposium on Image Analysis and Interpretation*, Mar. 28–30, 2004, pp. 196–200.
51. ——, "Real time AM-FM analysis of ultrasound video," in *45th Midwest Symposium on Circuits and Systems*, vol. 1, Aug. 4–7, 2002, pp. I–216–19.
52. P. Rodriguez V., M. Pattichis, M. Goens, and R. Abdallah, *M-Health: Emerging Mobile Health Systems*. Springer US, 2006, ch. Object-Based Ultrasound Video Processing for Wireless Transmission in Cardiology, pp. 491–507.
53. D. Gill, N. Gavrieli, and N. Intrator, "Detection and identification of heart sounds using homomorphic envelogram and self-organizing probabilistic model," in *Proc. Computers in Cardiology*, Sep. 25–28, 2005, pp. 957–960.
54. M. Pattichis, J. Ramachandran, M. Wilson, C. Pattichis, and P. Soliz, "Optimal scanning, display, and segmentation of the international labor organization (ILO) X-ray images set for pneumoconiosis," in *IEEE Symposium on Computer-Based Medical Systems*, 2001, pp. 511–515.
55. P. Soliz, M. S. Pattichis, J. Ramachandran, and D. S. James, "Computer-assisted diagnosis of chest radiographs for pneumoconioses," M. Sonka and K. M. Hanson, Eds., vol. 4322, no. 1. SPIE, 2001, pp. 667–675.
56. M. Pattichis, C. Pattichis, C. Christodoulou, D. James, L. Ketai, and P. Soliz, "A screening system for the assessment of opacity profusion in chest radiographs of miners with pneumoconiosis," in *IEEE Southwest Symposium on Image Analysis and Interpretation*, 7-9 April 2002, pp. 130–133.
57. D. C. Klonoff and D. M. Schwartz, "An economic analysis of interventions for diabetes." *Diabetes care*, vol. 23, pp. 390–404, Mar. 2000. [Online]. Available: http://www.hubmed.org/display.cgi?uids=10868871
58. C. Agurto, M. Pattichis, S. Murillo, V. Murray, M. Abramoff, S. Russell, E. Barriga, H. Davis, and P. Soliz, "Detection of structures in the retina using am-fm for diabetic retinopathy classification," in *2009 Meeting of the Association for Research in Vision and Ophthalmology*, May 2009.
59. TECHNO-VISION Project, "MESSIDOR: methods to evaluate segmentation and indexing techniques in the field of retinal ophthalmology." [Online]. Available: http://messidor.crihan.fr/

60. AREDS, "Areds database." [Online]. Available: http://eyephoto.ophth.wisc.edu/ResearchAreas/AREDS/AREDSstdPhotoIndex.htm
61. H. Kondo and T. Kouda, "Detection of pneumoconiosis rounded opacities using neural network," in *Joint 9th IFSA World Congress and 20th NAFIPS International Conference*, vol. 3, 25-28 July 2001, pp. 1581–1585.
62. ——, "Computer-aided diagnosis for pneumoconiosis using neural network," in *IEEE Symposium on Computer-Based Medical Systems*, 26-27 July 2001, pp. 467–472.
63. M. Pattichis, T. Cacoullos, and P. Soliz, "New models for region of interest reader classification analysis in chest radiographs," *Pattern Recognition*, vol. 42, no. 6, pp. 1058 – 1066, 2009, digital Image Processing and Pattern Recognition Techniques for the Detection of Cancer.
64. M. Pattichis, H. Muralldharan, C. Pattichis, and P. Soliz, "New image processing models for opacity image analysis in chest radiographs," in *IEEE Southwest Symposium on Image Analysis and Interpretation*, 7-9 April 2002, pp. 260–264.
65. B. Van Ginneken, B. M. Ter Haar Romeny, and M. Viergever, "Computer-aided diagnosis in chest radiography: a survey," *IEEE Transactions on Medical Imaging*, vol. 20, no. 12, pp. 1228–1241, December 2001.